

0017-9310(94)E0016-N

Three-dimensional laminar forced convection in a rotating square duct with a rib on the leading wall

SHOU-SHING HSIEH,[†] YING-JONG HONG and SHUENN-REN JENG

Department of Mechanical Engineering, National Sun Yat-Sen University, Kaohsiung, Taiwan 80424, Republic of China

(Received 21 April 1993 and in final form 29 December 1993)

Abstract—A 3-D numerical study on low speed forced convective heat transfer near a transverse rib in which the walls are subject to a constant heat flux in a rotating radial square duct is presented. The effects of Reynolds number and rotational Reynolds number as well as the entrance length of flow are examined and discussed. Flow field, temperature profiles, and local heat transfer coefficients were calculated for the entire domain of interest through the well-known SIMPLEC numerical scheme. Typical developments of axial velocity, secondary flow, and temperature at various axial positions near the rib in the entrance region are presented. Results indicate that the Nusselt number can be correlated in the following forms for fully developed region and entrance region, respectively:

$$\overline{Nu}_o = 0.65 Re^{0.36} Re_\Omega^{0.18} \text{ (fully developed region)}$$

$$\overline{Nu} = 1.04 Re^{0.31} Re_\Omega^{0.12} (Z/D)^{-0.21} \text{ (entrance region)}$$

Furthermore, a comparison of the present results with the available numerical data for stationary smooth duct is also presented.

INTRODUCTION

THE INCREASE in the turbine inlet temperature of gas turbine engines is an urgent need today to obtain a higher efficiency in the engines of aircraft, ships and on any other industrial occasions. Parallel with the evolution of metals working in high temperature, several methods of cooling rotor blades have been tried and developed. Cooled blades are widely used in modern engines. Commonly used methods are those of radial channel cooling. These channels are often designed with two artificially roughened and two smooth walls, and the designer must know the heat transfer coefficient on each of the walls in order to predict the turbine airfoil's life correctly. Naturally, it is also necessary to know the pressure loss for such a channel.

Work on fully developed turbulent flow in rough channels without rotation has received much attention (see, for example, refs. [1–4]). However, in actual operating conditions, the rotor blade is rotated at high speeds. In the presence of rotation, the Coriolis force generates secondary flows that can change the flow structure and heat transfer behavior significantly. There are many investigators who have studied flow and heat transfer characteristics in rotating radial smooth tubes/ducts, but only important numerical (or theoretical) literatures are reviewed here. Baura [5]

obtained an approximate series solution in a rotating pipe from a perturbation equation. The friction factor was then computed from the series solution. The results were valid only in the case of laminar flow with a small angular velocity. Mori and Nakayama [6] studied the laminar convective heat transfer in rotating radial circular ducts by assuming velocity and temperature boundary layers along the pipe wall. The friction factor and the Nusselt number were obtained in the region of large Re Re_Ω . Ito and Nanbu [7] studied extensively the friction factor for fully developed flow in smooth wall straight pipes of circular cross-section rotating at a constant angular speed about an axis perpendicular to its own for Reynolds numbers, ranging from 20 to 60 000. Empirical equations of the friction factors for small values of rotation Reynolds number were presented for both the laminar and turbulent flows. Hart [8] employed linear stability analysis for the laminar flow regime, and conducted an experiment for the onset of instability in a rotating channel flow. Skiadaressis and Spalding [9] predicted the flow and heat transfer characteristics for turbulent steady flow in a rectangular duct. Vidyanidhi *et al.* [10] substituted the theoretical velocity profiles, obtained by Barua [5] for an isothermal, developed flow, into the energy equation to determine the temperature profile for a uniformly heated wall case. Speziale and Thangam [11] numerically studied the pressure-driven laminar flow of an incompressible viscous fluid through a rec-

[†]Author to whom correspondence should be addressed.

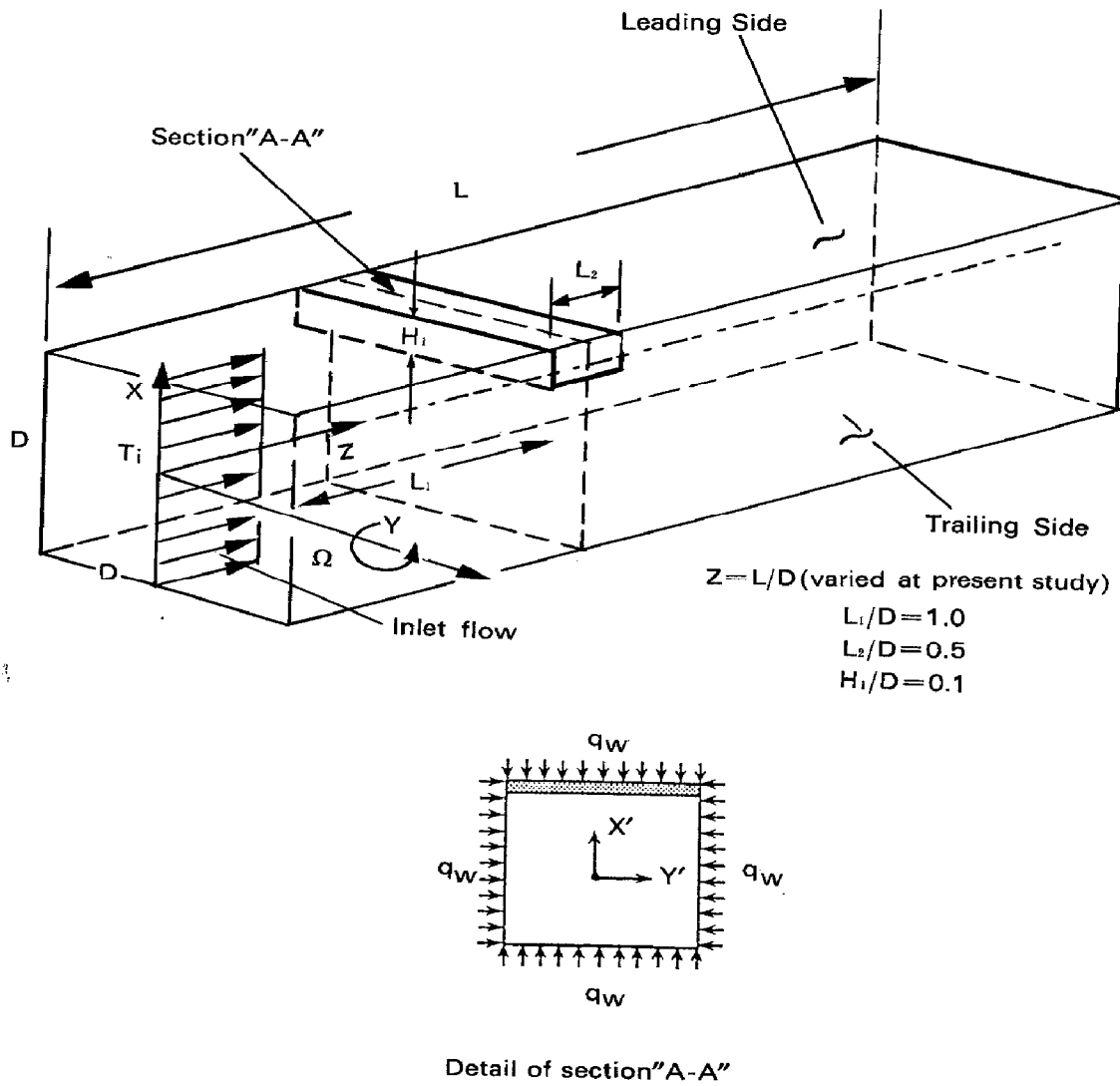


FIG. 1. Configuration and its dimension of the physical system.

energy. Because of the presence of the blockage, the flow is elliptic in nature. The incompressible flow is assumed to be steady, laminar and three-dimensional. These assumptions, for limited ranges of the governing parameter values, have been assumed in the literatures to be valid for smooth ducts [14]. Natural convection as well as radiation has been neglected in this study and therefore the results are applicable for moderate temperature difference. Since the values of $Pe (Re Pr)$ for the cases under investigation are between 75 and 400, axial conduction in the energy equation was also neglected.

The dimensionless variables chosen are :

$$\begin{aligned}
 X &= \frac{X'}{D} & Y &= \frac{Y'}{D} & Z &= \frac{Z'}{D} \\
 U &= \frac{U'}{\bar{W}} & V &= \frac{V'}{\bar{W}} & W &= \frac{W'}{\bar{W}} \\
 P &= P' / (\rho \bar{W}^2) & \theta &= \frac{T - T_i}{(q_w D) / k}
 \end{aligned}
 \tag{1}$$

The corresponding dimensionless governing equations are :

$$\frac{\partial U}{\partial X} + \frac{\partial V}{\partial Y} + \frac{\partial W}{\partial Z} = 0, \tag{2}$$

$$\begin{aligned}
 U \frac{\partial U}{\partial X} + V \frac{\partial U}{\partial Y} + W \frac{\partial U}{\partial Z} &= - \frac{\partial P}{\partial X} \\
 &+ \frac{1}{Re} \left(\frac{\partial^2 U}{\partial X^2} + \frac{\partial^2 U}{\partial Y^2} + \frac{\partial^2 U}{\partial Z^2} \right) - 2WRo,
 \end{aligned}
 \tag{3}$$

$$\begin{aligned}
 U \frac{\partial V}{\partial X} + V \frac{\partial V}{\partial Y} + W \frac{\partial V}{\partial Z} &= - \frac{\partial P}{\partial Y} \\
 &+ \frac{1}{Re} \left(\frac{\partial^2 V}{\partial X^2} + \frac{\partial^2 V}{\partial Y^2} + \frac{\partial^2 V}{\partial Z^2} \right),
 \end{aligned}
 \tag{4}$$

$$\begin{aligned}
 U \frac{\partial W}{\partial X} + V \frac{\partial W}{\partial Y} + W \frac{\partial W}{\partial Z} &= - \frac{\partial P}{\partial Z} \\
 &+ \frac{1}{Re} \left(\frac{\partial^2 W}{\partial X^2} + \frac{\partial^2 W}{\partial Y^2} + \frac{\partial^2 W}{\partial Z^2} \right) + 2URo,
 \end{aligned}
 \tag{5}$$

$$U \frac{\partial \theta}{\partial X} + V \frac{\partial \theta}{\partial Y} + W \frac{\partial \theta}{\partial Z} = \frac{1}{Re Pr} \left(\frac{\partial^2 \theta}{\partial X^2} + \frac{\partial^2 \theta}{\partial Y^2} \right), \quad (6)$$

where

$$Re = \bar{W}' D / \nu, \quad Re_\Omega = \Omega D^2 / \nu, \\ Ro = Re / Re_\Omega \quad \text{and} \quad Pr = \nu / \alpha.$$

The boundary conditions can be expressed as:

$$\langle 1 \rangle Y = 0$$

$$\frac{\partial U}{\partial Y} = 0 \quad V = 0 \quad \frac{\partial W}{\partial Y} = 0 \quad \frac{\partial \theta}{\partial Y} = 0, \quad (7)$$

$$\langle 2 \rangle Y = 0.5$$

$$U = V = W = 0 \quad \frac{\partial \theta}{\partial Y} = 1, \quad (8)$$

$$\langle 3 \rangle X = 0.5$$

$$U = V = W = 0 \quad \frac{\partial \theta}{\partial X} = 1, \quad (9)$$

$$\langle 4 \rangle X = -0.5$$

$$U = V = W = 0 \quad \frac{\partial \theta}{\partial X} = -1, \quad (10)$$

$$\langle 5 \rangle Z = 0$$

$$U = V = 0, \quad W = 1 \quad \theta = 0, \quad (11)$$

$$\langle 6 \rangle Z = Z_f (= \text{fully developed length})$$

$$\frac{\partial U}{\partial Z} = \frac{\partial V}{\partial Z} = \frac{\partial W}{\partial Z} = 0 \quad \frac{\partial \theta}{\partial Z} = \frac{4}{Re Pr}. \quad (12)$$

After the velocity and temperature fields are obtained, the computations of the local friction factor and Nusselt number are of practical interest. The local friction factor and Nusselt number are defined as follows:

$$f' = \frac{\tau_w}{\rho \bar{W}'^2 / 2} = -2\mu \left(\frac{\partial W'}{\partial n'} \right) / (\rho \bar{W}'^2) \\ = -2\mu \left[\left(\frac{\partial W'}{\partial n'} \right) / \left(\frac{\bar{W}'}{D} \right) \right] \left(\frac{\mu}{\rho \bar{W}' D} \right) \\ = -2 \left(\frac{\partial W'}{\partial n} \right) \frac{1}{Re}, \quad (13)$$

$$Nu = \frac{q_w D}{k[(T_w - T_b) - (T_{\min} - T_b)]} = \frac{1}{(\theta_w - \theta_{\min})}. \quad (14)$$

Here, T_{\min} and θ_{\min} represent the minimum temperature and dimensionless temperature, respectively, while n denotes the dimensionless coordinate normal to the wall.

The apparent Fanning friction factor is defined as:

$$f_{\text{app}} = \frac{\Delta P}{\rho \bar{W}'^2 / 2} \frac{D}{Z}. \quad (15)$$

Moreover, in order to investigate the heat transfer

from the rib surfaces (i.e. the front surface, top surface, and rear surface) separately, the quantity q/q_w (the heat transfer from the rib surface per unit area/the heat transfer from interior wall of the duct) is defined as:

$$q/q_w = -k \frac{\partial T}{\partial n'} / q_w = -k \frac{\partial(T - T_i)}{\partial(n'/D)} \frac{1}{q_w D} = -\frac{\partial \theta}{\partial n}. \quad (16)$$

An examination of dimensionless governing equations reveals four parameters: the Reynolds number (Re), the rotational Reynolds number (Re_Ω), the Rossby number (Ro) (dependent on Re , Re_Ω), and the Prandtl number (Pr). In the present study, the Prandtl number is assigned the value of 0.7 corresponding to air. The Reynolds number takes on values of 100, 200, 300, 400, and 500, and the rotational Reynolds number has the values of 5, 100, 200, 300, 400, and 500, while the Rossby number is varied between 0.01 and 5.

In addition to the aforementioned parameters, there are four geometrical parameters: L_1/D , L_2/D , H_1/D and L/D . The parameter L_1/D , has been assumed to be unity and L_2/D has the value of 0.5 while H_1/D , the dimensionless roughness (blockage) height, is assigned the value of 0.1 and L/D is chosen to be sufficiently far downstream so that the outflow boundary condition is satisfied. Furthermore, the length for fully developed flow was studied. In summary, Table 1 lists the present physical geometry and relevant parameters under consideration.

The partial differential equations are solved using an adaptation of the implicit, elliptic, finite difference scheme called SIMPLEC (Semi Implicit Method for Pressure Linked Equations, Consistent) set forth in ref. [15]. It is found that numerical solutions are sensitive to the grid distribution as well as to the grid size. Various non-uniform grid systems are tested for $17 \times 22 \times 57$, $27 \times 32 \times 62$, and $32 \times 37 \times 72$, respectively. A choice of the final grid distribution, $27 \times 32 \times 62$, is sufficient to provide a friction factor at fully developed regime less than 4% difference for both ducts with/and without a rib on one wall between the grid layouts of $27 \times 32 \times 62$ and $27 \times 32 \times 72$ which can be seen from Table 2. The finest grid, of dimension $0.02H_1$ is located adjacent to the wall, and the sizes of other grids are chosen such that each is within 125% of the adjacent grid (based on trial and error procedure) in order to avoid abrupt changes and to obtain convergence. The calculations are started at a distance of one duct height upstream of the rib. Based on several test runs, the downstream distance was set having 20 duct heights (namely, $Z = 20$). It will be verified later that this value is long enough to guarantee all the cases considered reaching thermally fully developed.

The numerical procedure is based on an iterative scheme. The hybrid central/upwind difference scheme is used for diffusion and convective terms. The set of

Table 1. Geometry parameters and boundary conditions

Parameters	Rib height, H_1	$0.1D$
	Distance from duct inlet, L_1	$1.0D$
	Rib width, L_2	$0.5D$
	Reynolds number, Re	100, 200, 300, 400, 500
	Rotational Reynolds number, Re_Ω	5, 100, 200, 300, 400, 500
Boundary conditions	Rossby number, Ro	0.01–5
	$Y = 0$	$\partial U/\partial Y = 0, V = 0, \partial W/\partial Y = 0, \partial \theta/\partial Y = 0$
	$Y = 0.5$	$U = V = W = 0, \partial \theta/\partial Y = 1$
	$X = 0.5$	$U = V = W = 0, \partial \theta/\partial X = 1$
	$X = -0.5$	$U = V = W = 0, \partial \theta/\partial X = -1$
	$Z = 0$	$U = V = 0, W = 1, \theta = 0$
	$Z = Z_r^\dagger$	$\partial U/\partial Z = \partial V/\partial Z = \partial W/\partial Z = 0, \partial \theta/\partial Z = 4/Re Pr$

$^\dagger Z_r$ was determined based on test runs.

differential equations over the entire region of interest is solved by obtaining new values for any desired variables, taking into account the latest known estimated values of the variable from the neighboring nodes. One iteration process is complete when, in line-by-line technique, all the lines in a chosen direction have been accounted for. Because of the large variations in the source terms, under-relaxation was necessary for the dependent variables and the source terms to achieve convergence [15]. Line inversion iteration with typical under-relaxation values of 0.5 for velocity terms and 0.7 for the pressure correction term were incorporated to the facilitated calculation. These values are within the range recommended by Patankar [16]. A variable G is said to be convergent if its residual is smaller than a pre-assigned value. The residual is defined as

$$\beta = \max \left| \frac{G^n - G^{n+1}}{G^n} \right|_{ij},$$

where n refers to the n th iteration and i, j stand for the node position. In the above expression, the residual β ($= 10^{-6}$ for present study) represents the maximum values throughout the computational region. Selection of the value of β takes into account the fact that the rather strong under-relaxation leads to small changes from iteration step to iteration step. In addition, the converged velocity field had to satisfy

continuity within prescribed error, both locally (at each control volume) and globally (the mass flow rate calculated at any cross-section of the channel, such as the inlet and the outlet, had to be constant). The present numerical calculation was performed on an IBM PC/80486. Typical computation times were approximately 8000–9000 CPU seconds.

RESULTS AND DISCUSSION

Numerical results were obtained for: (1) the local velocity components and temperature; (2) the local Nusselt number distributions along the rib surfaces; (3) the local Nusselt number on the leading wall; and (4) the circumferentially-averaged Nusselt number. In the interest of brevity, only selected results will be presented. Results presented include: (1) the velocity vector (secondary flow) and dimensionless temperature distribution (isothermal patterns) in the channel cross-section; (2) the constant axial velocity profile; (3) the axial velocity and dimensionless temperature profiles at the center of the channel cross-section; (4) the local Nusselt number on the leading wall; and (5) the circumferentially-averaged Nusselt number. Moreover, smooth duct results will be also provided for a comparison under certain conditions. Finally, a comparison of the present results with previous investigations is presented. The Reynolds num-

Table 2. Conservation of energy and mass flux examination for different grid layouts

Re	Re_Ω	Conservation of energy		
		$17 \times 22 \times 57$	$27 \times 32 \times 62$	$32 \times 37 \times 72$
100	5	3.35%	1.08%	0.69%
	500	4.13%	1.09%	0.60%
500	5	3.47%	1.10%	0.80%
	500	4.26%	1.21%	0.72%
Re	Re_Ω	Conservation of mass flux		
		$17 \times 22 \times 57$	$27 \times 32 \times 62$	$32 \times 37 \times 72$
100	5	0.17%	0.15%	0.14%
	500	0.47%	0.39%	0.36%
500	5	0.26%	0.22%	0.21%
	500	0.65%	0.53%	0.50%

ber and rotational Reynolds number are varied for laminar flow of air ($Pr = 0.7$) through the channel with isoflux walls. For a total of 30 cases studied herein, Table 3 gives the fully developed length needed and the salient features regarding the rotating square duct flow over isolated rib on one wall. It is clearly noted that the size of the reattachment bubble as well as the distance between the center of the bubble and rear wall of the rib get bigger and longer, respectively, as Re/Re_Ω increases.

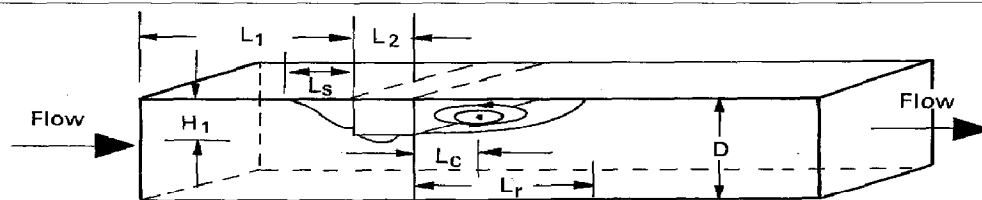
Due to the term $2WRo$ on the right-hand side of equation (2), the Coriolis force drives the flow in the negative X -direction and is non-uniformly distributed on the cross-section. The term $2URo$ in equation (5) is also the Coriolis force from the product of X -direction velocity and angular velocity. It is well recognized [11] that a square duct without a rib is rotating at a constant speed about the Y -axis, and the fluid in the core region is driven by the Coriolis force acting in the negative X -direction. Consequently, the fluid in the core region then pushes the fluid near the side walls to the positive X -direction and a pair of counter-rotating eddies which are known as Taylor vortices (or Dean type cells) are thus generated. In the present numerical study, the flow pattern changes are found with a rib positioned at downstream station (L_1/D) on one wall.

As stated earlier, the actual form of the primary flow regime depends on the values of Ro and rib geometry. A secondary (transverse) flow with its origin is the non-uniform distribution of the Coriolis force in the direction parallel to the axis of rotation, which develops in the duct. The actual form of the primary flow regime depends on the values of Re , Ro and rib geometry. However, it is possible to distinguish the following major characteristics of the restructuring of the flow due to the present rotational effect and roughened surface geometry. The secondary flow takes the form of a vortex pair symmetrical about the plane of $Y = 0$ without a rib/or block. With a block/rib located in the downstream distance on one wall, the pattern of this secondary flow is dramatically distorted and broken. The secondary (transverse) flow

caused by the velocity components U and V along the downstream distance near a rib wall at five locations is clearly examined in Fig. 2. The single pair of secondary flow cells existing in a conventionally radially rotating square duct no longer exists. Instead, the flow towards the negative X -direction was influenced by the presence of the rib with a low Ro . This influence becomes less obvious as the flow moves far away from the rib and, in turn, it results in a small vortex in the bottom half of the flow passage as evidenced in Fig. 2a for $Z = 0.9$ and 1.0. An examination of Fig. 2a for $Z = 1.3$, where the flow has just passed over the middle top floor, shows that, at this position, the movement to the negative X -direction of the flow near the left top of the wall and the top floor of the rib becomes less noted. In addition, due to the solid wall, the magnitude of this movement decreases owing to this combining effect. The flow patterns at this position are quite similar to those of radially rotating ducts without a rib/block. But, in the core region, the effect of the negative X -direction movement still stands. After the flow passes over the entire rib (i.e. $Z = 1.5$ and 1.6 in Fig. 2a), due to the absence of the rib, the flow moves towards the positive X -direction again. Moreover, near the upper solid wall, the flow velocity decreases and, hence, the effect of rotation becomes the major factor to affect the entire flow pattern in such a way that the core flow moves back toward the symmetrical axis. On the contrary, when Ro gets a larger value ($Ro = 1.667$), an extreme rotational effect makes the present flow pattern in Fig. 2b look like the secondary flow found in a smooth duct reported by Lei and Hsu [17] again. Besides, in Fig. 2b for $Z = 0.9-1.3$ due to the rib, the flow still moves in the negative X -direction a bit. This can be seen from the larger magnitude of the secondary velocity vector ($\sqrt{U^2 + V^2}$) on the upper half near the symmetrical axis. In Fig. 2b for $Z = 1.5$ and 1.6, the core region is still occupied by a single bubble. However, as stated earlier in Fig. 2a for $Z = 1.5$ and 1.6, the flow moves in the positive X -direction again in the top region with the absence of the rib. Com-

Table 3. Relevant parameters (L_s/H_1 , L_c/H_1 , L_r/H_1 , Z_r) of the rib when flow passing over

Re	Re_Ω	L_s/H_1	L_c/H_1	L_r/H_1	Z_r
100	5	0.8098	1.4714	9.4785	15.8325
	500	0.8094	1.5101	9.5989	15.9788
300	5	1.3235	3.2863	12.1749	17.3324
	500	1.3239	3.3147	12.1820	18.0132
500	5	1.9966	5.8234	14.9275	18.5408
	500	1.9967	5.8354	14.9541	18.9632



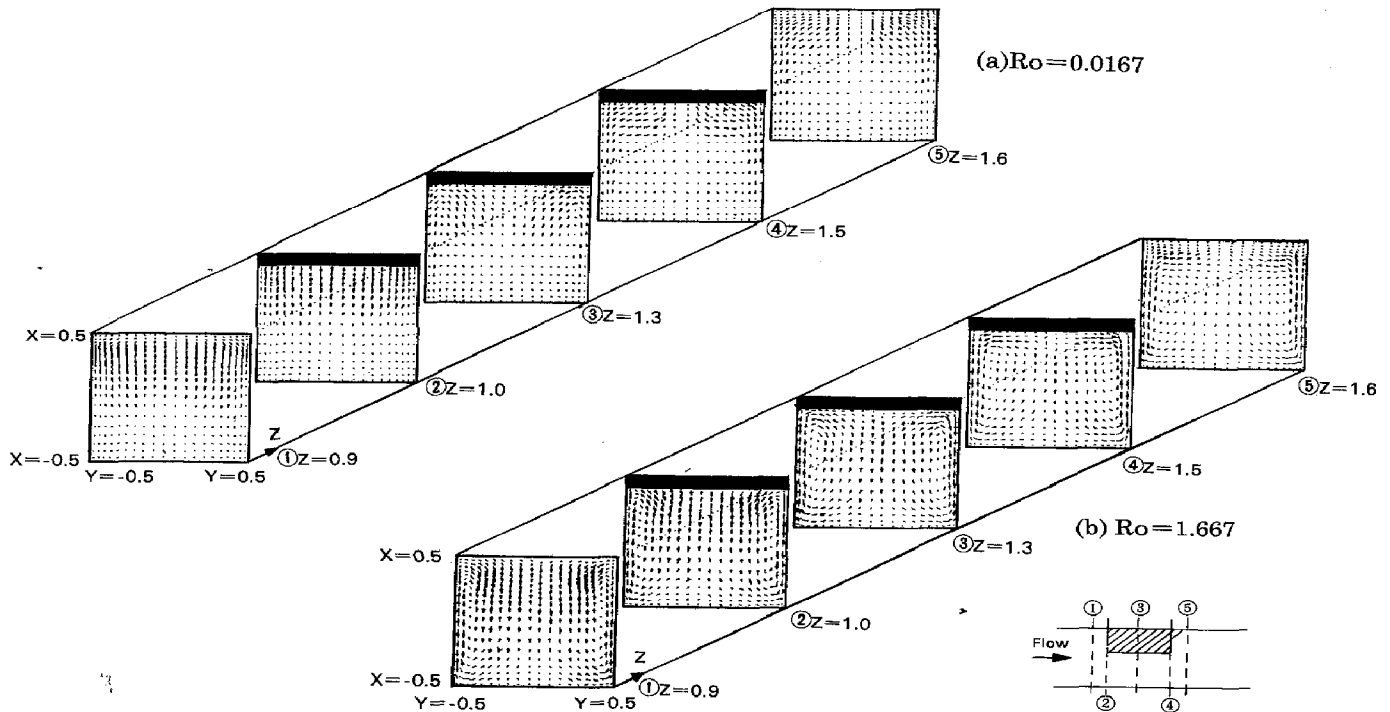


FIG. 2. Secondary flow patterns at various axial stations for: (a) $Ro = 0.0167$ ($Re = 300$, $Re_{\Omega} = 5$); and (b) $Ro = 1.667$ ($Re = 300$, $Re_{\Omega} = 500$).

paring Fig. 2a and b, it indicates that the strength of the secondary flow at each downstream station becomes larger as Ro increases whether the rib exists or not.

To understand the relation between the flow field and heat transfer characteristics, the isovels and the corresponding isotherms should be examined simultaneously. Figure 3 displays the cross-sectional contours of dimensionless isotherms and isovels of some cases at the same locations as shown in Fig. 2a and b, respectively, with indices designating the magnitude of θ and W . Due to the nature of the symmetry, the isotherms and isovels are plotted separately in the left and right halves of ducts. It is seen that, due to rotation, a Coriolis force is imposed on each fluid element, which results in a fluid element with a high velocity, occurring in the central region, moving faster than those around the near wall region and hence forced to move by the incoming fluid towards the trailing wall. It is for this reason that the peak of the constant axial velocity is shifted to the trailing half of the channel cross-section. The higher the rotational speed, the larger the shift, as shown in Fig. 3. Moreover, with increasing rotational Reynolds number the change in pattern and the progress of the maximum velocity towards the trailing wall is much more apparent at the immediate front/rear (i.e. $Z = 0.9$ and 1.6) of the rib than on the top (i.e. $Z = 1.0, 1.3$ and 1.5) of it. This is to be expected since the Coriolis force is the vector product of the duct rotation vector and the relative flow field. The axial velocity changes (axial velocity gradients) are large along the trailing and side walls, i.e. lower velocities prevail in the leading half

of the channel cross-section (positive X region) while the trailing half has higher velocities. This is true except for the locations near the rib where, due to the suddenly reduced area of the cross-section, the flow passing over the rib is accelerated. This is very similar to the phenomena observed in the stationary duct with a rib mounted on one wall. Consequently, the effect of rotation becomes the minor factor to affect the entire flow pattern. As can also be seen from these figures, the isovels are seen to be parallel to the bottom wall (trailing wall) and typical boundary-layer flow phenomena occur over the side walls. Similar flow mechanisms have been observed in curved ducts [18].

The consequence of this complex flow structure results in a complicated thermal profile. The strength distribution of the thermal fluid is opposite to that in the fluid flow field. The region of high velocity, where most heat is convected away by the fluid, is the region of lower temperature (Fig. 3). Lower temperatures prevail in the trailing half of the channel cross-section except in the narrow region adjacent to the wall, where temperature changes (i.e. thermal gradients) are steep, resulting in a higher heat transfer. The sparse existence of isotherms in the vicinity of the leading wall means that a substantially lower heat transfer occurs there. A deviation in the isotherm distribution from that of no rotation (i.e. a symmetrical distribution of isotherms around all four walls) is a measure of the effect of rotation.

Generally speaking, the distribution of the axial velocity component (W) in Fig. 4 exhibits that in the vicinity of the leading wall the transition to flow with Taylor vortices is accompanied by the development

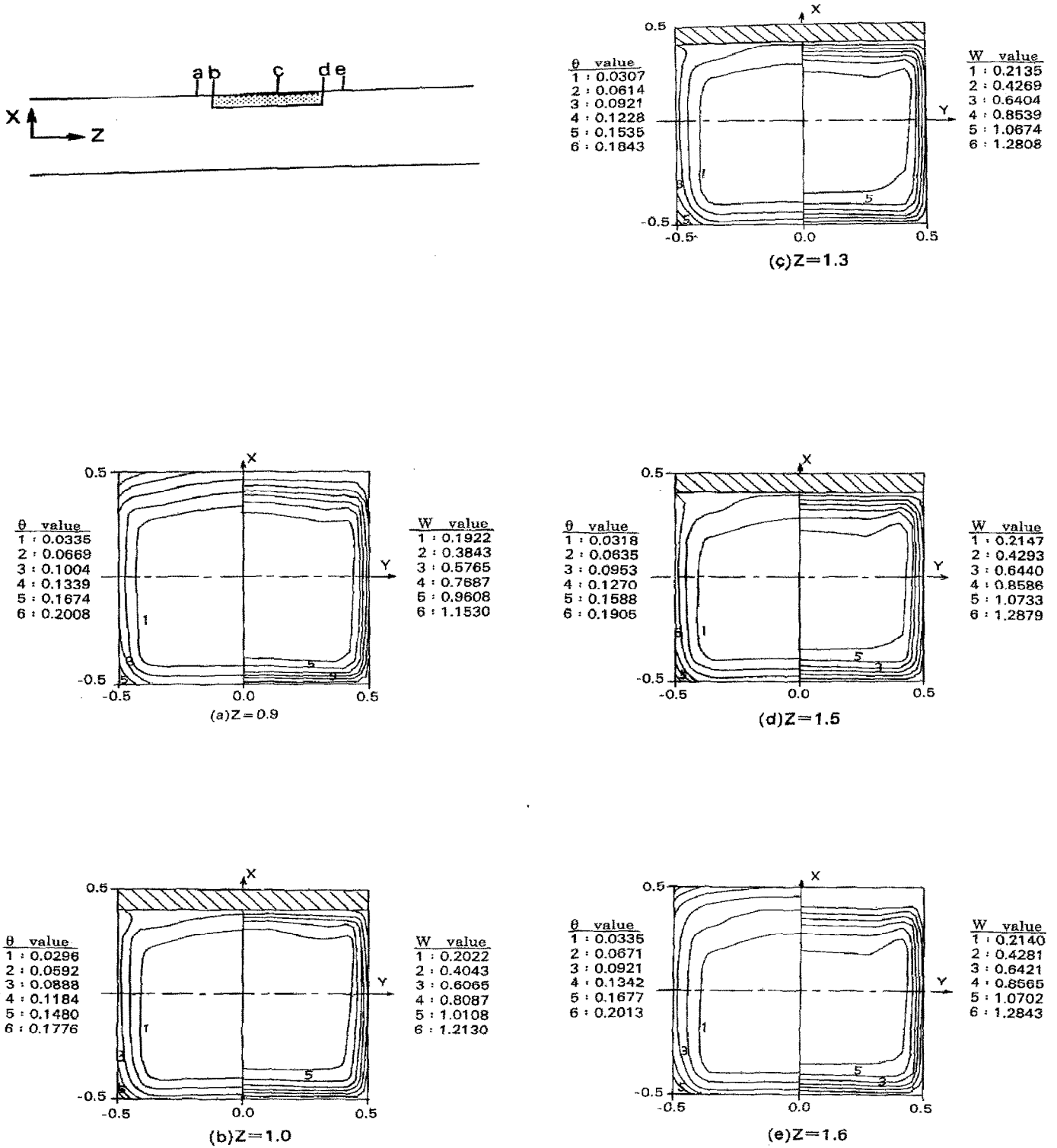


FIG. 3. Constant axial velocity (W) and isotherms (θ) for roughened duct at $Re = 300$ and $Re_\Omega = 500$.

of a deep trough in the $W(X)$ profiles. Obviously, this is due to decelerated fluid being carried from the wall into the flow.

Figure 4a shows the axial velocity profile along symmetric plane for $Ro = 0.0167$ ($Re = 300, Re_\Omega = 5$) at different downstream stations $Z = 0.9, 1.3, 1.6$ and 20 . The flow pattern is skewed continuously from the

parabolized profile (Hagen–Poiseuille). The profile at $Z = 20$ is exactly the same as that of the smooth duct for the fully developed result. This is quite obvious because at $Z = 20$, from Table 3, it is found that when $Z \geq 18.1$ the flow was fully developed. Moreover, it indicates that there is no significant influence at $Z = 20$ due to the presence of the rib. However, the

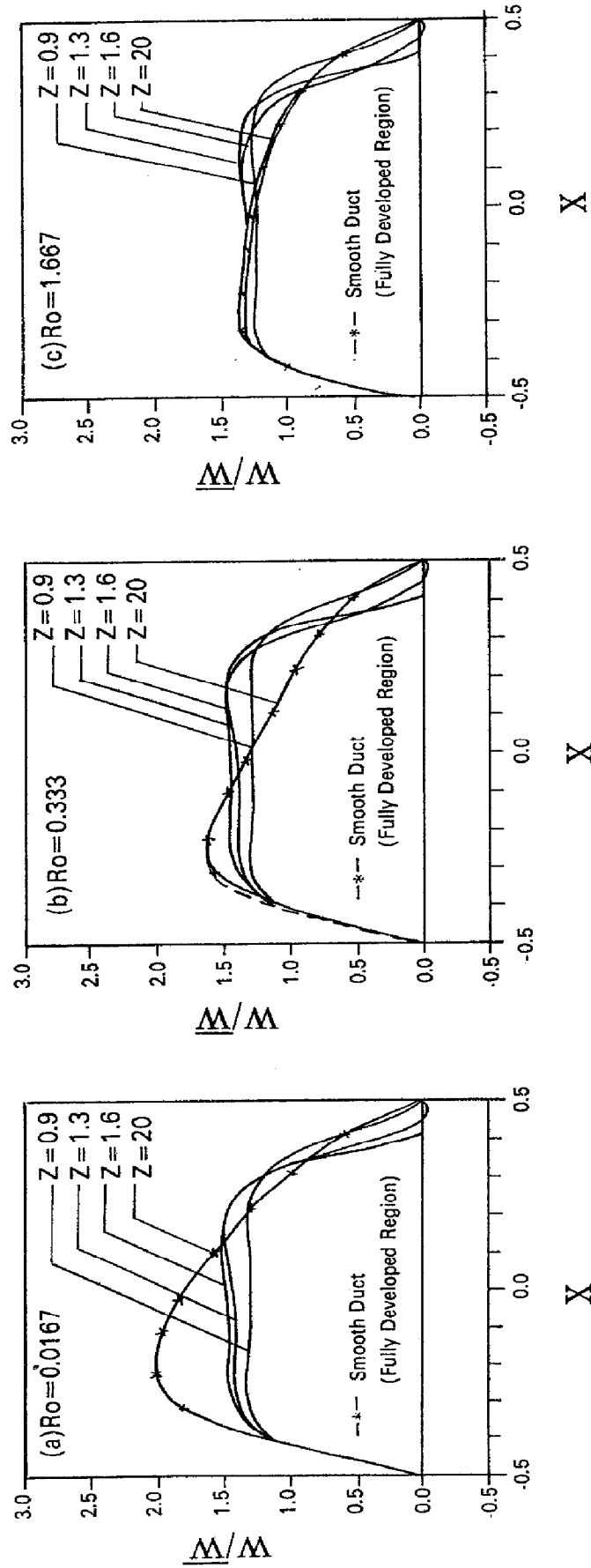


FIG. 4. Variation of the axial velocity profile along the X -axis at $Re = 300$: (a) $Ro = 0.0167$; (b) $Ro = 0.333$; and (c) $Ro = 1.667$.

rib does affect the flow pattern a lot when the flow is at $Z = 0.9, 1.3$ and 1.6 . It appears that the velocity profile shows a flat region, i.e. $W \neq W(X)$ in $-0.4 \leq X \leq 0.4$, with a rib compared with that without a rib. This means that near the vicinity of the rib the flow pattern becomes less skewed. The biggest departure from the smooth data was found at $Z = 0.9$ (upstream of the rib). Besides, it should be noted that the axial velocity gradient on the trailing wall $(\partial u/\partial x)_{x=-0.5}$ grows steep far from the rib, while that on the leading wall $(\partial u/\partial x)_{x=0.5}$ diminishes. This observation has two important implications. One has to do with the friction performance: higher values of the local friction factor on the trailing wall and lower values on the leading wall in the region far from the rib. But, adjacent to the vicinity of the rib, the local friction factor on the trailing wall is equal to that on the leading wall. The other is the physical phenomenon referred to as Ekman flow, in which the main flow stream is directed toward the trailing wall instead of moving parallel to the channel axis. This phenomenon was also observed in a radially outward flow through rotating parallel disks [19] and, consequently, it enhances the convection heat transfer performance. Figure 4b and c shows the same plot to observe the effect of rotation increases for $Ro = 0.333$ ($Re = 300$, $Re_\Omega = 100$) and $Ro = 1.667$ ($Re = 300$, $Re_\Omega = 500$), respectively. This behavior can be clearly noted in Fig. 4c as the effect of the rotation further increases. As one can observe, the discrepancy among those four downstream locations becomes less distinguishable as the rotational Reynolds number is increased to $Ro = 1.667$. It indicates that the effect of rotation nearly removed the influences of the rib.

The location of the W_{\max} shifts toward the trailing wall, $X = -0.5$, at $Ro \leq 0.33$ ($X = -0.2$, $Ro = 0.0167$ and $X \approx -0.3$, $Ro = 0.333$). However, W_{\max} is not easily noted for $Ro = 1.667$ in the present study due to the rib effect becoming dominant as Z increases from 0.9 to 1.6. Actually, W_{\max} is hardly found for a smooth duct/or smooth floor. On the contrary, it happens right on the top floor of the rib ($Z = 1.3$ in present study) when Ro is small ($Ro \leq 0.333$). The value of W_{\max} becomes small as the effect of rotation is further increased.

The profiles of $W(X, 0, 1.6)$ and $\theta(X, 0, 1.6)$ are shown in Fig. 5 when curves are shown for $Ro = 0.0167, 0.333$, and 1.667 . These graphs enable one to infer the effect of Re_Ω on the main flow for a constant value of the parameter $Re = 300$ behind the rib. As can be seen from Fig. 5a, for these rotational Reynolds numbers, the recirculating flow exists in the downstream region of the rib with the same reverse flow velocities. Due to the present asymmetry in nature (only one rib positioned on the wall) and rotational effect the flow was redistributed and, then, a double-peak profile occurs. This phenomenon is mainly caused by the flow being accelerated as it passes through the rib and by the shift in the axial velocity due to rotation. It can also be seen from Fig. 5a

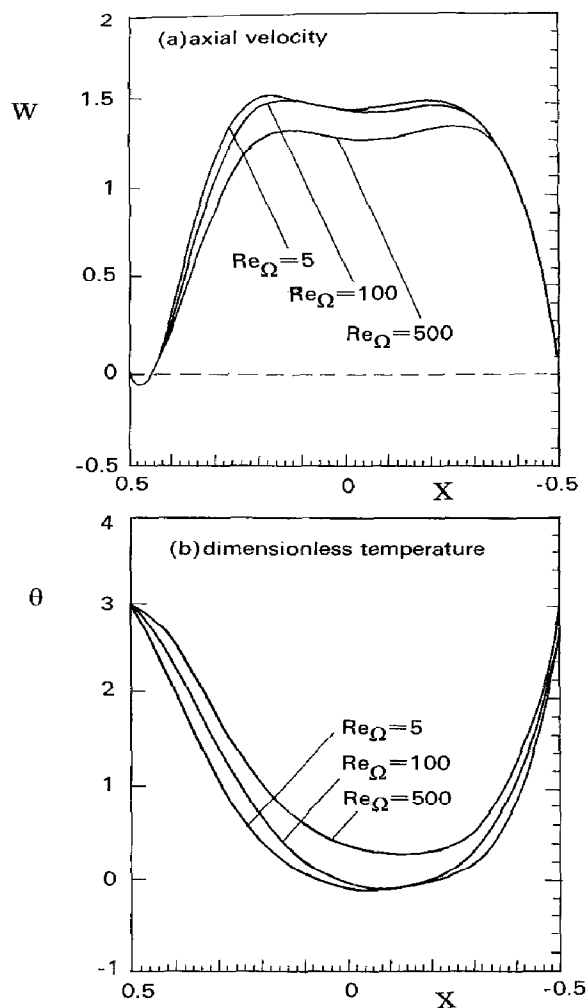


FIG. 5. Effect of rotational Reynolds number (Re_Ω) on variation of: (a) axial velocity; and (b) dimensionless temperature profiles at channel center ($Y = 0$) at $Z = 1.6$ for $Re = 300$.

that, when Ro is increased, the core is decelerated and reduced in size. This is because the Coriolis force acting in the upstream direction [cf. equation (5)] becomes stronger due to the stronger downward (negative- X) secondary flow, and a decrease in peak velocity is observed. A deformation in the axial velocity profile results in similar characteristics for the dimensionless temperature profile, as shown in Fig. 5b. It should be noted that the temperature gradient on the leading wall grows steep as Re_Ω increases. This is the mechanism of heat transfer enhancement on the leading wall due to rotation.

The local heat flux and normalized Nusselt number (Nu/Nu_0) along the rib surface for various Reynolds number and rotational Reynolds number are shown in Fig. 6. The rib perimeter has been expanded linearly along the abscissa of the figure. Because the present study is a 3-D problem naturally, the data for the local heat flux are presented at three different transverse positions [i.e. $Y = 0.13, 0.28$, and 0.45 (near the right side wall), respectively]. To confirm this, attention is drawn to the fact that q/q_w drops below zero near

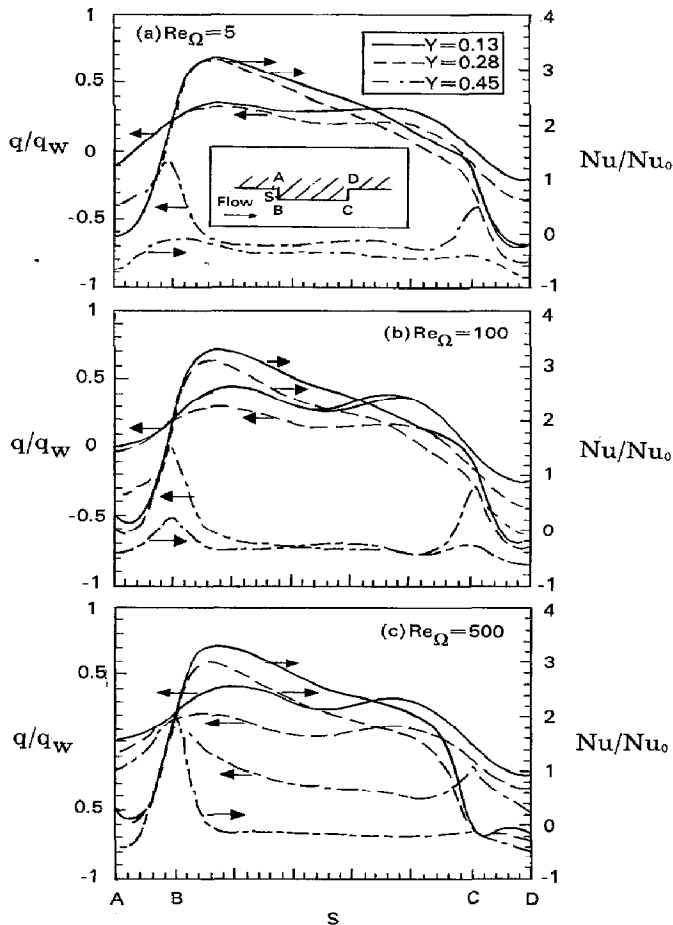


FIG. 6. Local heat flux and Nusselt number at three different transverse positions for various rotational Reynolds number at $Re = 300$.

points A (the upstream concave corner) and D (the downstream concave corner). At these locations, where the fluid is nearly stagnant, the direction of energy flow is actually from the fluid to the solid rib wall. It should be noted that the conductivity of the rib is much larger than that of the working fluid (it is assumed that $k_{rib}/k_{air} = 100$ in the present study). The highest heat transfer occurs on the upstream side of the rib and at the rib tip where the influence of the high impingement velocities is most pronounced. The local heat flux drops rapidly on the downstream side of the rib where recirculation velocities are low. These phenomena are also observed in Webb and Ramadhani [20] for laminar air flow through a parallel plate channel with staggered, transverse ribs.

It can be seen from Fig. 6 that all the values of the local heat flux for $Y = 0.45$ are smaller than those for $Y = 0.13$ and $Y = 0.28$. This is due to the fact that the region at $Y = 0.45$ embedded in the thermal boundary layer causes this region to have a lower heat flux. It should be noted that, for $Y = 0.45$, the heat fluxes on the upstream side, the top wall, and the downstream side have worse values than the others.

As can also be seen from Fig. 6, taking $Y = 0.13$ for example, the heat flux increases along the front

face, giving the largest value at the end of the face (the upstream protruding corner, B). The heat flux then decreases in magnitude until the flow reached the end of the top surface of the rib (C). At the downstream protruding corner (C) the local heat flux rises a little bit due to the cellular motion. Then it decreases again, prior to the region of the redevelopment of the boundary layer, along the downstream side wall. The mechanism of heat transfer between the rearward side of the rib and the recirculation zone is mainly by conduction. Taking a closer examination of Fig. 6, as the rotational Reynolds number is increased at a fixed Reynolds number, the effect of the rotational speed is more significant at $Y = 0.45$ than at $Y = 0.13$ and 0.228. This is because the axial velocity near the right side wall is promoted as the rotational Reynolds number is increased. The local heat flux is therefore increased. Similar distributions of normalized Nusselt number have been observed in Fig. 6.

The locally circumferentially averaged heat transfer coefficients (\overline{Nu}) are obtained, and it varies depending upon the leading, trailing and side walls. But only the data on the leading wall (the side mounted with one rib) are presented here. Figure 7a–c depicts the effects of Re on the axial variation of Nusselt number at various rotational Reynolds number. Previous investigations [14] on a stationary smooth duct are also plotted for comparison. As shown in Fig. 7, \overline{Nu} takes a steep fall near the entrance due to the present inlet boundary conditions, until it reaches the rib. A strong resemblance is observed between the local heat flux in Fig. 6 and the locally averaged Nusselt number in Fig. 7 on the forward-facing side, the top wall, and the rearward-facing side of the rib. As the flow passed over the rib, a sharp decline in \overline{Nu} is followed by a smooth, gradual recovery at $Re = 100$. As Re is increased to 300 and 500, a decline in \overline{Nu} is followed by a smooth first. Then a gradual bump occurs once Re_{Ω} exceeds 100. This bump can be attributed to the reversal of the trailing wall temperature (not shown here) caused by the emergence of secondary vortices. As flow proceeds downstream, the Nusselt number then flattens toward its fully developed value at $Z \geq 20.0$. Figure 7 further depicts the effects of Re_{Ω} on the axial Nusselt number distributions. The increase in heat transfer in the entrance region due to the effect of rotation is insignificant as observed in Fig. 7a–c. Moreover, it indicates that at low rotational speeds (e.g. $Re_{\Omega} = 5$), \overline{Nu} firstly takes a lower value near the recirculation zone than that of a stationary smooth duct as reported in [14]. Then, a slight augmentation is found at the region far from the rib. Generally, the enhancement of heat transfer from $Re_{\Omega} = 100$ to $Re_{\Omega} = 500$ is not as impressive as the increase from $Re_{\Omega} = 5$ to $Re_{\Omega} = 100$.

Figure 8 compares the present study with the available results in the literature for the uniform wall temperature and heat flux cases. \overline{Nu}_0 is defined as the integrated mean value of the heat transfer coefficients, \overline{Nu} , on the leading side over the square flow channel

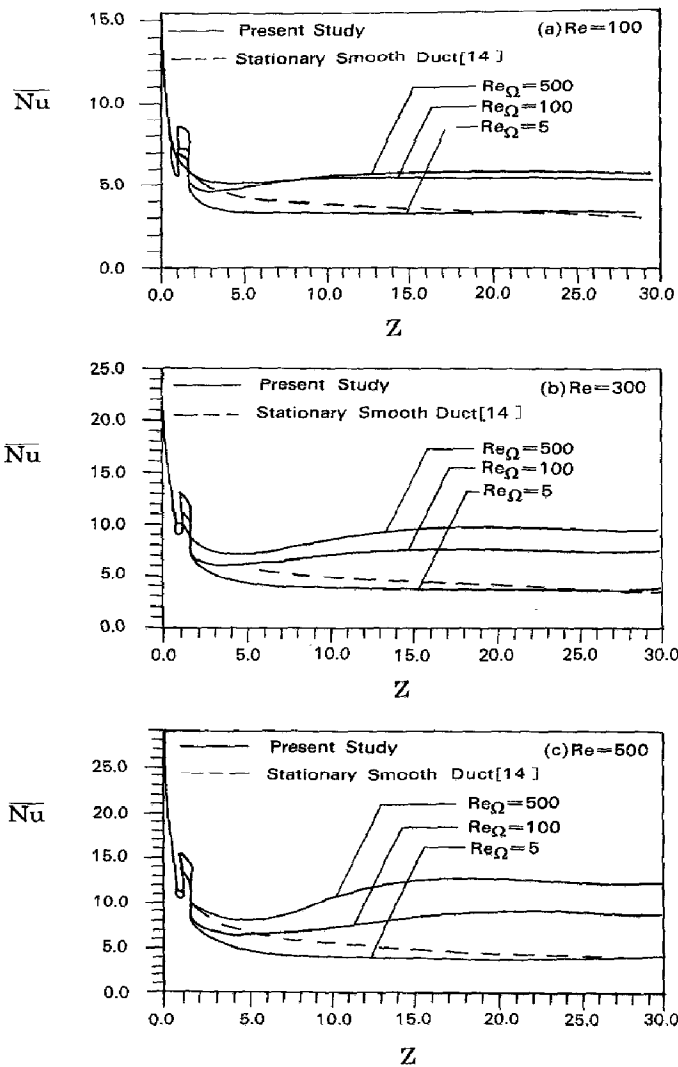


FIG. 7. Nu vs Z at different rotational Reynolds numbers.

with $L/D = 30$ from $Z = 0$ to $Z = 30$. It is plotted against $Re Pr Re_{\Omega}$. Superimposed on the figure for comparison are results from the existing literature for rotating smooth duct, including numerical results for isothermal circular tubes [21], numerical results for fully developed flow in isothermal square channels [13], and analytical curves for fully developed flow in circular tubes with isoflux walls [6]. It is seen that the value of \overline{Nu}_o increases with an increase in $Re Pr Re_{\Omega}$. It is also found that, in comparison with the empirical correlation [21], the present results show a superior role for all cases except at the lower rotational speeds (e.g. $Re Pr Re_{\Omega} < 500$) as far as the heat transfer rate is considered. This is expected, because the present study deals with a roughened duct with developing velocity and temperature for which the separation/reattachment and entrance effects result in higher heat transfer performance.

CONCLUDING REMARKS

The problem of hydrodynamically and thermally developing flow through a rotating channel with a rib mounted on leading wall and uniform heat flux at four walls has been investigated numerically. The nature of the rib was positioned at $Z/D = 1.0$ from the duct inlet with the rib geometry of $L_1/D = 1.0$, $L_2/D = 0.5$, and $H_1/D = 0.1$. Owing to the presence of a rib on the top wall (leading wall) of the channel, the present numerical calculation was a three-dimensional problem. Illustrations describing the flow field and heat transfer characteristics are constructed for $100 \leq Re \leq 500$, and $5 \leq Re_{\Omega} \leq 500$ to broaden our fundamental understanding of this type of channel flow. The most important features can be described as follows.

- (1) The secondary flow takes the form of a vortex

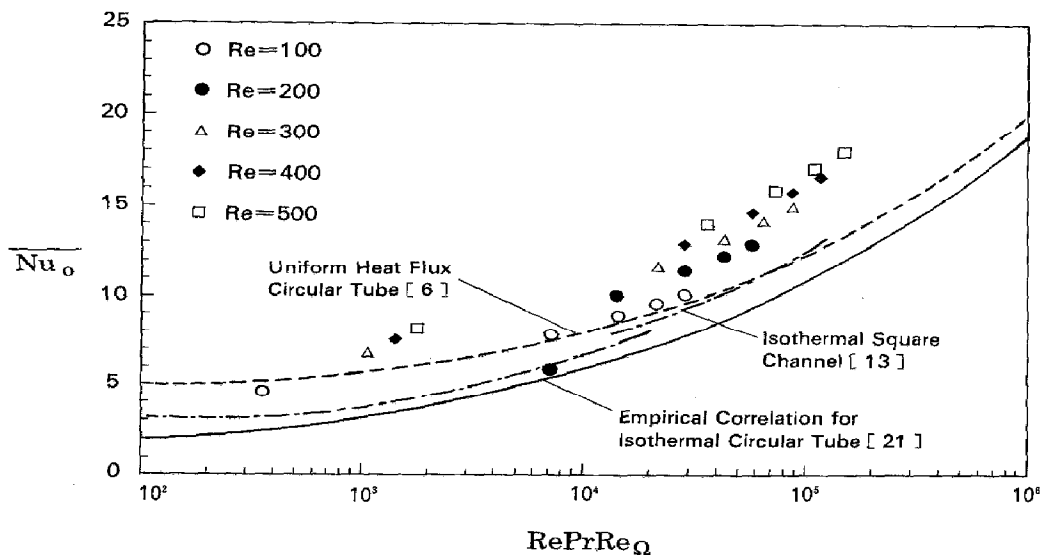


FIG. 8. Comparison of present results with existing literature.

pair symmetrical about the plane of $Y = 0$ without a rib. However, with a rib located in the downstream distance, the pattern of the secondary flow is dramatically distorted and broken down. When the effect of rotation was weak, the flow moves towards the negative X -direction by presence of the rib. But the flow moves far away from the rib. It results in a small vortex in the bottom half of the channel. Meanwhile, in the flow field behind the rib, due to the absence of the rib, the flow moves back toward the positive X -direction. When the effect of rotation becomes stronger, the secondary flow patterns look like the secondary flow found in a smooth duct.

(2) The local heat flux (q/q_w) drops below zero near points A (the upstream concave corner) and D (the downstream concave corner). At these locations, where the fluid is nearly stagnant, the direction of energy flow is actually from the fluid to the solid rib. The highest transfer occurs on the upstream side of the rib and the rib tip where the influence of the high impingement velocities is most pronounced. The local heat flux drops rapidly on the downstream side of the rib where recirculation velocities are low.

(3) The locally circumferentially averaged heat transfer coefficients (\overline{Nu}) on the leading wall (the side mounted with one rib) takes a steep fall near the entrance, until it reaches the rib. As the flow passed over the rib, a sharp decline in \overline{Nu} is followed by a smooth, gradual recovery at $Re = 100$. As Re is increased to 300 and 500, a decline in \overline{Nu} is followed by a smooth part: then a gradual bump occurs once Re_Ω exceeds 100. As flow proceeds downstream, the Nusselt number then flattens again toward its fully developed value at $Z \geq 20.0$. Besides, the increase in heat transfer in the entrance region due to the effect of rotation is insignificant. It is also revealed that the enhancement of heat transfer from $Re_\Omega = 100$ to $Re_\Omega = 500$ is not as impressive as the increase from $Re_\Omega = 5$ to $Re_\Omega = 100$.

(4) In general, \overline{Nu}_o are augmented with an increase in the rotational speed (Re_Ω) and Reynolds number (Re). For a specified Reynolds and rotational Reynolds number, for instance $Re = 500$ and $Re_\Omega = 500$, an enhancement about 3 times higher than a stationary smooth duct in heat transfer coefficient due to rotation is observed.

Acknowledgement—Revision assistance of this paper from Mr. Chun-Jen Weng is gratefully appreciated.

REFERENCES

1. R. J. Boyle, Heat transfer in serpentine passages with turbulence promoters, *ASME Paper No.84-HT-24* (1984).
2. S. S. Hsieh and Y. J. Hong, Separating flow over repeated surface mounted-ribs in a square duct, *AIAA J.* **27**, 770–776 (1989).
3. Y. J. Hong and S. S. Hsieh, An experimental investigation of turbulent flow over staggered ribs in a square duct, *Experimental Thermal Fluid Sci.* **4**, 714–722 (1991).
4. R. E. Mayle, Pressure loss and heat transfer in a channels roughened on two opposed walls, *J. Turbomachinery* **113**, 60–66 (1991).
5. S. N. Barua, Secondary flow in a rotating straight pipe, *Proc. R. Soc. (A)* **227**, 133–139 (1954).
6. Y. Mori and W. Nakayama, Convection heat transfer in rotating radial circular pipe (1st report, laminar region), *Int. J. Heat Mass Transfer* **11**, 1027–1040 (1968).
7. H. Ito and K. Nanbu, Flow in rotating straight pipe of circular cross section, *J. Basic Engng* **93**, 383–394 (1971).
8. J. E. Hart, Instability and secondary motion in rotating channel flow, *J. Fluid Mech.* **45**, 341–351 (1971).
9. D. Skiadaressts and D. B. Spalding, Heat transfer in a pipe rotating around a perpendicular axis, *ASME Paper, No. 77-WA/HT-39* (1977).
10. V. Vidyanidhi, V. V. S. Suryanarayana and V. C. Chenchu Raju, An analysis of steady fully developed heat transfer in a rotating straight pipe, *ASME J. Heat Transfer* **117**, 148–150 (1977).
11. C. G. Speziale and Thangam, Numerical study of secondary flow and roll-cell instabilities in rotating channel flow, *J. Fluid Mech.* **130**, 337–395 (1983).
12. H. S. Khesghi and L. E. Scriven, Viscous flow through a rotating square channel, *Phys. Fluid* **28**, 2968–2979 (1985).
13. G. J. Hwang and T. C. Jen, Convective heat transfer in rotating isothermal duct, *Int. J. Heat Mass Transfer* **33**, 1817–1828 (1990).
14. R. K. Shah and A. K. London, Laminar flow forced convection in ducts, Supplement 1 to *Advances in Heat Transfer*. Academic Press, New York (1978).
15. J. P. Van Doormaal and G. D. Raithby, Enhancements of the SIMPLE method for predicting incompressible fluid flows. *Numer. Heat Transfer* **7**, 147–163 (1984).
16. S. V. Patankar, *Numerical Heat Transfer and Fluid Flow*. Hemisphere, Washington, DC (1980).
17. U. Lei and C. H. Hsu, Flow through rotating straight pipes, *Phys. Fluid (A)* **2**, 63–75 (1990).
18. K. H. Winters, A bifurcation study of laminar flow in a curved tube of rectangular cross-section, *J. Fluid Mech.* **180**, 343–369 (1987).
19. Y. S. Sim and W. J. Yang, Numerical study on heat transfer in laminar flow through co-rotating parallel disks, *Int. J. Heat Mass Transfer* **27**, 1963–1970 (1984).
20. B. W. Webb and S. Ramadhyani, Conjugate heat transfer in a channel with staggered ribs, *Int. J. Heat Mass Transfer* **28**, 1679–1687 (1985).
21. Y. Mori, T. Fukada and W. Nakayama, Convective heat transfer in rotating circular pipe (2nd report), *Int. J. Heat Mass Transfer* **14**, 1807–1824 (1971).